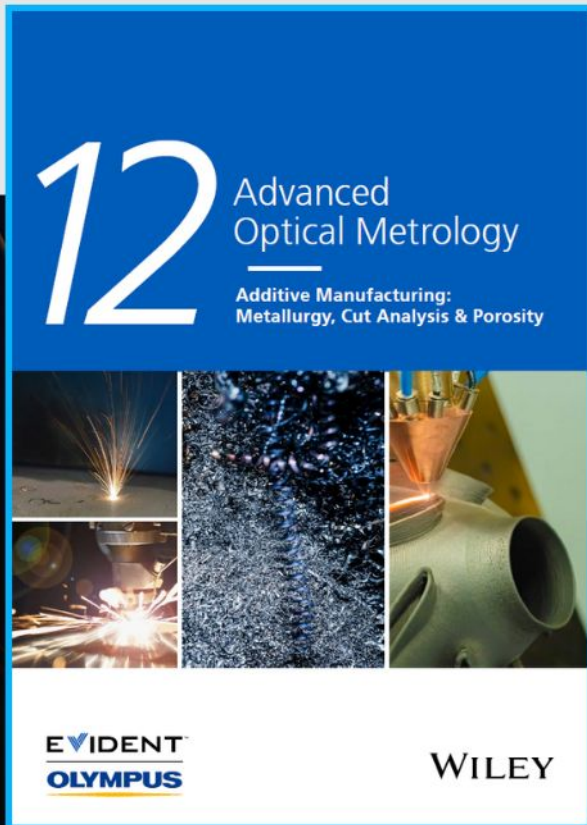




Additive Manufacturing: Metallurgy, Cut Analysis & Porosity



The latest eBook from
Advanced Optical Metrology.
Download for free.

In industry, sector after sector is moving away from conventional production methods to additive manufacturing, a technology that has been recommended for substantial research investment.

Download the latest eBook to read about the applications, trends, opportunities, and challenges around this process, and how it has been adapted to different industrial sectors.

EVIDENT
OLYMPUS

WILEY

Low-Energy Hydrogen Ions Enable Efficient Room-Temperature and Rapid Plasma Hydrogenation of TiO₂ Nanorods for Enhanced Photoelectrochemical Activity

Xiaodan Wang,^{*} Leonhard Mayrhofer, Martin Keunecke, Sonia Estrade, Lluís Lopez-Conesa, Michael Moseler, Andreas Waag, Lothar Schaefer, Weidong Shi, Xiangjian Meng, Junhao Chu, Zhiyong Fan,^{*} and Hao Shen^{*}

Hydrogenation is a promising technique to prepare black TiO₂ (H-TiO₂) for solar water splitting, however, there remain limitations such as severe preparation conditions and underexplored hydrogenation mechanisms to inefficient hydrogenation and poor photoelectrochemical (PEC) performance to be overcome for practical applications. Here, a room-temperature and rapid plasma hydrogenation (RRPH) strategy that realizes low-energy hydrogen ions of below 250 eV to fabricate H-TiO₂ nanorods with controllable disordered shell, outperforming incumbent hydrogenations, is reported. The mechanisms of efficient RRPH and enhanced PEC activity are experimentally and theoretically unraveled. It is discovered that low-energy hydrogen ions with fast subsurface transport kinetics and shallow penetration depth features, enable them to directly penetrate TiO₂ via unique multiple penetration pathways to form controllable disordered shell and suppress bulk defects, ultimately leading to improved PEC performance. Furthermore, the hydrogenation-property experiments reveal that the enhanced PEC activity is mainly ascribed to increasing band bending and bulk defect suppression, compared to reported H-TiO₂, a superior photocurrent density of 2.55 mA cm⁻² at 1.23 V_{RHE} is achieved. These findings demonstrate a sustainable strategy which offers great promise of TiO₂ and other oxides to achieve further-improved material properties for broad practical applications.

1. Introduction


Hydrogenation has emerged as an attractive approach for the synthesis of H-TiO₂ with remarkable material properties for clean hydrogen production by solar-driven water splitting.^[1–12] However, the widespread application of H-TiO₂ is limited by the harsh conditions of conventional hydrogenation processes: thermal molecular or atomic hydrogenations are widely used,^[4–6] but suffer from high temperatures and prolonged treatment times due to energetically and kinetically unfavorable processes at the microscopic level, which requires thermal activation to overcome energy barriers to diffuse sluggishly into the TiO₂ subsurface. More specifically, we demonstrated using density functional theory (DFT) calculations, that in the case of molecular hydrogenation, the hydrogen chemisorption and formation of oxygen vacancies are thermally activated processes, and also atomic hydrogen uptake in the rutile TiO₂ subsurface proceeding

X. Wang, M. Keunecke, L. Schaefer, H. Shen
Fraunhofer Institute for Surface Engineering and Thin Films
Bienroder Weg 54E, 38108 Braunschweig, Germany
E-mail: w.xiaodan@outlook.com; hshen678@126.com

L. Mayrhofer, M. Moseler
Fraunhofer Institute for Mechanics of Materials IWM
Wöhlerstraße 11, 79108 Freiburg, Germany

S. Estrade, L. Lopez-Conesa
Department d'Electrònica
Universitat de Barcelona
c/Martí Franquès 1, Barcelona 08028, Spain

A. Waag
Institute for Semiconductor Technology
TU Braunschweig
Hans-Sommer-Strasse 66, 38106 Braunschweig, Germany

 The ORCID identification number(s) for the author(s) of this article can be found under <https://doi.org/10.1002/sml.202204136>.

W. Shi
School of Chemistry and Chemical Engineering
Jiangsu University
Xuefu Road 301, Zhenjiang 212013, China

X. Meng
Shanghai Institute of Technical Physics
Chinese Academy of Sciences
Yu Tian Road 500, Shanghai 200083, China

J. Chu
Institute of Optoelectronics
Fudan University
Song Hu Road 2005, Shanghai 200438, China

Z. Fan
Department of Electronic and Computer Engineering
The Hong Kong University of Science and Technology
Clear Water Bay, Kowloon, Hong Kong SAR 999077, China
E-mail: eezfan@ust.hk

DOI: 10.1002/sml.202204136

via the $O_{3c} \rightarrow O_{sub}$ low-energy-barrier pathway requires thermal activation.^[6] Therefore, high temperatures are required in case of both atomic and molecular hydrogenation approaches which are thus incompatible with practical applications.

Using kinetic rather than thermal hydrogen species, plasma hydrogenation has attracted recent attention because it does not rely on thermal activation. But conventional plasma hydrogenation again suffers from high temperature or from the high power set by the plasma equipment producing the high-energy hydrogen ions, causing inefficient and uncontrollable hydrogenation.^[12–16] Additionally, the highest photocurrent density of 0.9 mA cm⁻² at 1.23 V_{RHE} reported to date for plasma-based H-TiO₂ is relatively low.^[14] Simultaneously, the underlying mechanism of plasma hydrogenation has not yet been reported due to the complexity of the hydrogen species involved in the process.

We develop a room-temperature and rapid plasma hydrogenation (RRPH) strategy to enable hydrogen ions with relatively low kinetic energies using a circular electromagnetic coil to synthesize H-TiO₂ nanorods with a controllable disordered shell. We systematically investigate the mechanisms of RRPH and enhanced photoelectrochemical (PEC) activity by combining experimental measurements with DFT calculations. We study the influence of RRPH on the structural, optical, electrical, and PEC properties of H-TiO₂ and reveal that the kinetic low-energy hydrogen ions trigger a narrower bandgap and larger band bending, along with the suppression of bulk defects to improve electron–hole pair generation, charge transport, and charge injection. In this way, we achieve improved PEC activity, yielding a higher photocurrent density of 2.55 mA cm⁻² at 1.23 V_{RHE} than previously reported H-TiO₂. The findings observed experimentally are consistent with our theoretical studies: the efficient RRPH and enhanced PEC performance are ascribed to kinetic low-energy hydrogen ions exhibiting fast subsurface transport kinetics and shallow penetration depth. This allows direct hydrogen ion penetration of the TiO₂ surface, the formation of a controllable disordered shell and finally the suppression of the formation of bulk defects. In summary, we demonstrate an efficient RRPH strategy to fabricate H-TiO₂ nanorods with enhanced PEC performance owing to kinetic low-energy hydrogen ions.

2. Results and Discussion

2.1. The RRPH Strategy

The novel RRPH strategy we have developed as a highly efficient hydrogenation method for practical applications is schematically shown in **Figure 1a**. Unlike conventional plasma hydrogenation, the RRPH is realized by integrating a circular electromagnetic coil in the substrate electrode of a radio frequency (RF) plasma physical vapor deposition (PVD) set-up to produce a magnetic field, which can increase the density of hydrogen ions, decrease RF power and self-bias voltage, resulting in controllable kinetic low-energy hydrogen ions (**Figures S1 and S2**, Supporting Information). Experimentally, a low self-bias voltage (V_{bias}) of –250 V was obtained by applying a RF powering of the substrate of 20 W during the

RRPH process. Correspondingly, this leads to an upper limit of 250 eV for the kinetic energy of the plasma hydrogen ions (**Table S1**, Supporting Information). In the control plasma process without using the circular electromagnetic coil, we found that hydrogen plasma cannot be created by applying a RF power of 20 W under the same process conditions, indicating the important role of the circular electromagnetic coil that leads to controllable low-energy hydrogen ions while maintaining the hydrogen plasma. In contrast with conventional plasma hydrogenation, our RRPH enables low-energy hydrogen ions to successfully prepare H-TiO₂ nanorods with the best photocurrent density without the need of high power or high temperature (**Table S2**, Supporting Information).

2.2. Hydrogenation-Property Experiments

To study the influence of RRPH on the structural, optical, electrical, and PEC properties of H-TiO₂ nanorods, we fabricated H-TiO₂ nanorods samples using treatment times of 2.5, 5, 10, 20, and 40 min, respectively (**Table S1**, Supporting Information).

To measure the morphological and phase changes of TiO₂ before and after RRPH treatment, we performed scanning electron microscopy (SEM) and X-ray diffraction (XRD) measurements. The SEM images of pristine TiO₂ and H-TiO₂ at 5 min show no morphological change (**Figure S3a,b**, Supporting Information), and no appreciable difference in morphology of H-TiO₂ samples was observed. The XRD patterns of pristine TiO₂ and H-TiO₂ samples show only rutile phase with (101) and (002) peaks (JCPDS No. 89-0920), no additional phases were identified (**Figure S4**, Supporting Information), indicating no phase change of TiO₂ before and after RRPH treatment.

To further quantify the microstructural change of pristine TiO₂ and H-TiO₂, we carried out transmission electron microscopy (TEM) and electron energy loss spectroscopy (EELS) experiments. **Figure 1b–j** shows the TEM and high-resolution transmission electron microscopy (HR-TEM) images of pristine TiO₂ and H-TiO₂ samples, and **Figure 1d** shows the fast Fourier transformation (FFT) converted from **Figure 1c**. It indicates the single-crystalline feature of pristine TiO₂ nanorods with [001] growth direction and {110} sidewalls. Compared to the pristine TiO₂, H-TiO₂ samples are composed of a crystalline core and a disordered shell structure, and the FFT image indicates that the core structure of H-TiO₂ remains single-crystalline (**Figure 1g**), whereas the shell thickness is ≈2 nm for H-TiO₂ treated at 5 min (**Figure 1f**) and increases to 5 nm for H-TiO₂ treated at 40 min (**Figure 1i**). **Figure 2a–f** shows the line-scan EELS which provides the change of [O]/[Ti] ratio of pristine TiO₂ and H-TiO₂ samples across the crystalline core and disordered shell interface. The [O]/[Ti] ratio of H-TiO₂ at both 5 and 40 min gradually decreases in the shell range (**Figure 2e,f**), indicating the formation of oxygen vacancies in the shell. Moreover, the [O]/[Ti] ratio in the core range of H-TiO₂ at 5 min is ≈2.25 (**Figure 2e**) identical to pristine TiO₂ (**Figure 2d**). Hence, it is evident that no oxygen vacancies are formed in the bulk, whereas the [O]/[Ti] ratio decreases to 1.7 for H-TiO₂ at 40 min (**Figure 2f**), indicating that more oxygen vacancies are formed in the bulk region.

To determine the composition of the disordered shell, we conducted X-ray photoelectron spectroscopy (XPS) analysis.

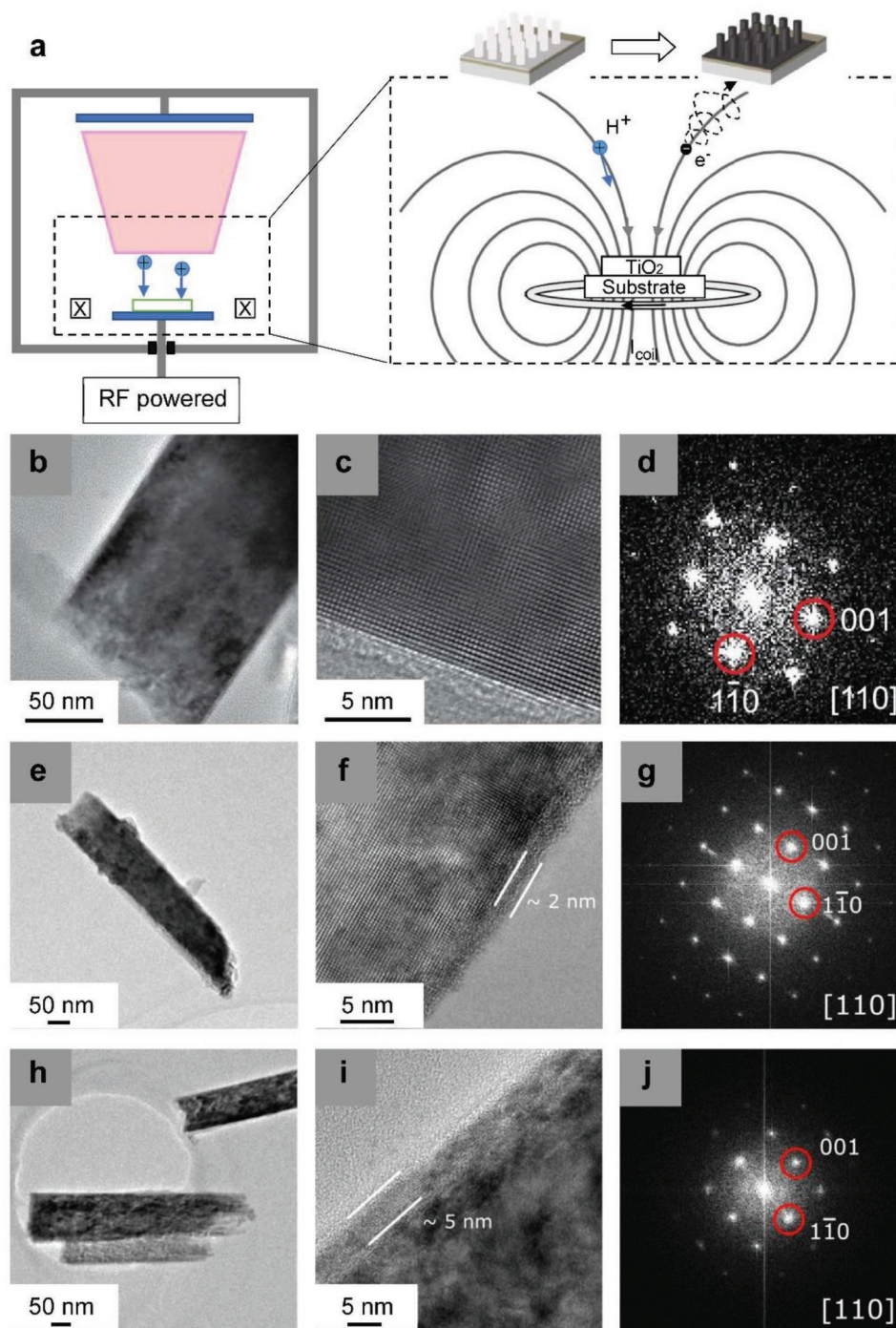


Figure 1. a) Experimental set-up of magnetic-field-assisted RRRP. TEM, HR-TEM, and FFT images of b–d) pristine TiO₂ and H-TiO₂ at e–g) 5 and h–j) 40 min, respectively.

Figure 2g shows that the O 1s spectra of pristine TiO₂ and H-TiO₂ at 5 and 40 min, respectively. The O 1s peak at 530 eV is attributed to Ti–O, whereas the peak at 531.5 eV is assigned to Ti–OH, indicating the formation of Ti–OH in the shell of H-TiO₂. Figure 2h shows the Ti 2p spectra of pristine TiO₂ and H-TiO₂ at 5 and 40 min, respectively. It is noted that Ti³⁺ is formed in the H-TiO₂ at 5 min, and strong reduction

(Ti⁴⁺ → Ti³⁺ → Ti²⁺) has occurred in the H-TiO₂ at 40 min, revealing that the higher concentration of Ti³⁺ is obtained in the disordered shell of H-TiO₂ at 5 min.

To understand the optical properties of pristine TiO₂ and H-TiO₂, we measured UV–vis absorption spectra. Figure S5a (Supporting Information) shows that the absorption band edges of H-TiO₂ are redshifted, and the absorption in the visible to

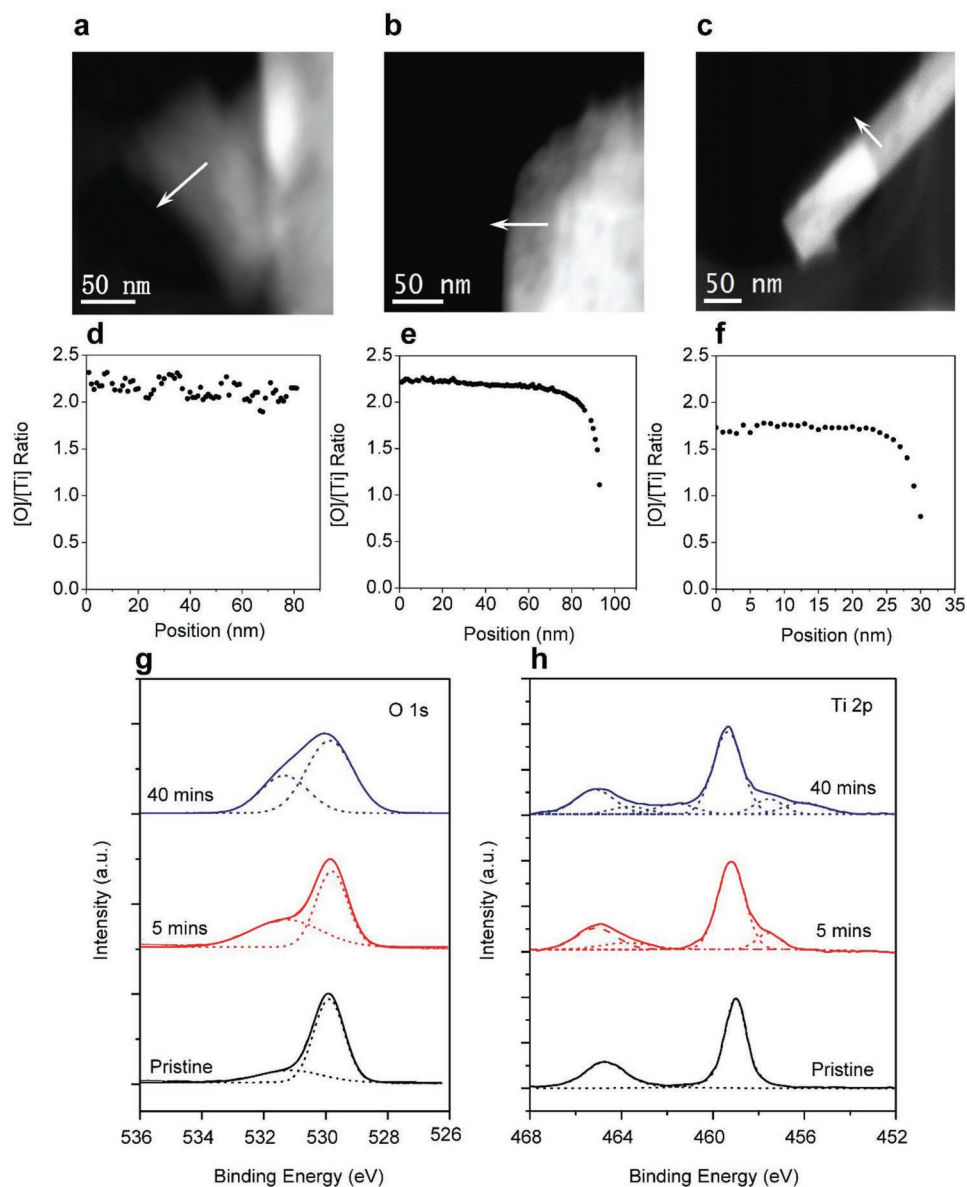


Figure 2. STEM HAADF images for the a) pristine TiO₂ and H-TiO₂ at b) 5 and c) 40 min, respectively. The arrows correspond to the directions along which spatially localized EEL spectra were acquired. d–f) [O]/[Ti] composition ratios for the three cases, obtained from the quantification of the acquired spectra. g,h) O 1s and Ti 2p XPS spectra of pristine TiO₂ and H-TiO₂ at 5 and 40 min, respectively.

infrared range gradually increases with increased treatment time. The Tauc plot demonstrates the bandgap narrowing from 3.0 eV of pristine TiO₂ to 2.91 eV of H-TiO₂ at 5 min (Table 1; and Figure S5b, Supporting Information).

To evaluate the influence of RRP treatment time on the PEC properties of H-TiO₂, we performed the measurements of the photocurrent density versus potential (*J*–*V*) and incident photon-to-current efficiency (IPCE). Figure 3a,b indicates the enhancement of photocurrent density of H-TiO₂ as the treatment time increases up to 5 min, but decreasing when the treatment time is longer than 5 min. At 5 min, the photocurrent density of 2.55 mA cm⁻² at 1.23 *V*_{RHE} is achieved, which is the best value among the reported H-TiO₂ studies (Table S3, Supporting Information). The trend of IPCE (Figure S6,

Supporting Information) is consistent with that observed in the *J*–*V* curves. In comparison to pristine TiO₂, the IPCE of H-TiO₂ is enhanced in the range of 300–420 nm. It is evident that H-TiO₂ at 5 min achieves the highest IPCE whereas the IPCE of H-TiO₂ decrease with increasing the treatment time over 5 min.

To clarify the impact of RRP treatment on the donor density (*N*_d), depletion region width (*W*), and flat band potential (*V*_{fb}) of H-TiO₂, we recorded the Mott–Schottky (*M*–*S*) plots (Figure 3c) with following Equations (1)–(3)

$$\frac{1}{C^2} = \frac{2}{e_0 \epsilon_0 \epsilon_r N_d} \left(V - V_{fb} - \frac{kT}{e_0} \right) \quad (1)$$

Table 1. Summary of hydrogenation-property experiments.

Treatment time [min]	0	2.5	5	10	20	40
Disordered shell thickness [nm]	0	–	2	2	–	5
[O]/[Ti] ratio in the core range	2.25	–	2.25	–	–	1.7
Bandgap [eV]	3.0	2.91	2.91	2.91	2.908	2.908
J [mA cm ⁻²] at 1.23 V _{RHE}	0.63	2.01	2.55	2.05	1.68	1.19
N_d [cm ⁻³]	1.50×10^{17}	1.36×10^{19}	3.02×10^{19}	5.48×10^{19}	4.01×10^{20}	6.45×10^{20}
W [nm] at 1.23 V _{RHE}	312	34	23	16	5.9	4.7
V_{fb} [V _{RHE}]	-0.09	-0.15	-0.30	-0.10	-0.05	-0.02
V_{sc} [V]	0.89	0.95	1.10	0.90	0.85	0.82

$$N_d = \left(\frac{2}{e_0 \epsilon_0 \epsilon_r} \right) \left[\frac{d(1/C^2)}{dV} \right]^{-1} \quad (2)$$

$$W = \sqrt{\frac{2\epsilon_0 \epsilon_r (V - V_{fb})}{e N_d}} \quad (3)$$

where C is the capacitance, e_0 is the electron charge, ϵ_0 is the permittivity of vacuum, ϵ_r is the dielectric constant of TiO₂, N_d is the donor density, V is the applied potential, V_{fb} is the flat band potential, k is the Boltzmann constant, T is the temperature, and W is the depletion region width. It is evident that increasing the treatment time leads to an increase in N_d but a decrease in W (Figure 3d), the corresponding values of N_d and W are identified at different treatment time (Table 1). Additionally,

the V_{fb} of pristine TiO₂ and H-TiO₂ were identified by M–S plots (Inset, Figure 3c). Compared with pristine TiO₂, the negative shift of V_{fb} of H-TiO₂ at 2.5 and 5 min, respectively, is attributed to the substantially increased donor density (Table 1), which consequently shifts the Fermi level (E_F) toward the conduction band (E_C). The V_{fb} of H-TiO₂ increases from -0.30 V_{RHE} at 5 min to -0.10, -0.05, and -0.02 V_{RHE} at 10, 20, and 40 min, respectively. This shift is ascribed to oxygen vacancies in the bulk of H-TiO₂ when the treatment time is longer than 5 min. We determined the band bending (V_{sc}) by V_{fb} from M–S plots (Figure 3c and Table 1),^[15] the largest band bending of 1.1 V is achieved for H-TiO₂ at 5 min.

The hydrogenation-property experiments reveal that the best photocurrent density of H-TiO₂ at 5 min is primarily attributed to the following factors: i) XPS shows the higher concentration of

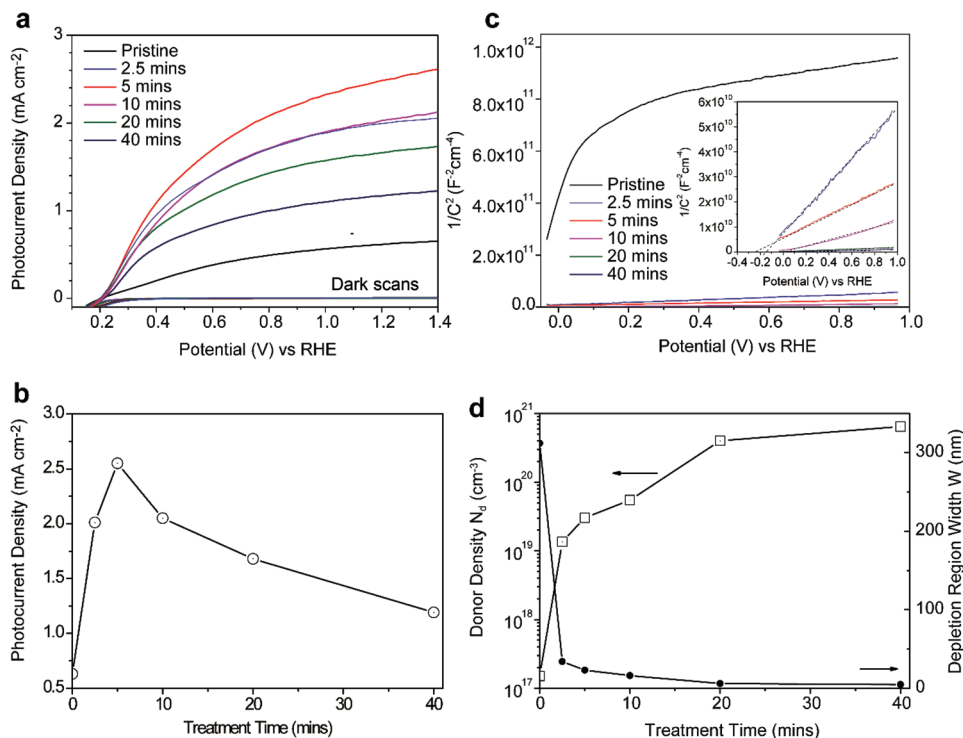


Figure 3. a) J – V curves of pristine TiO₂ and H-TiO₂ at different treatment times in 1 M KOH solution in the dark and under solar illumination. b) Treatment time-dependent photocurrent density of H-TiO₂. c) M–S plots of pristine TiO₂ and H-TiO₂ at different treatment times. d) Treatment time-dependent donor density and depletion region width of H-TiO₂.

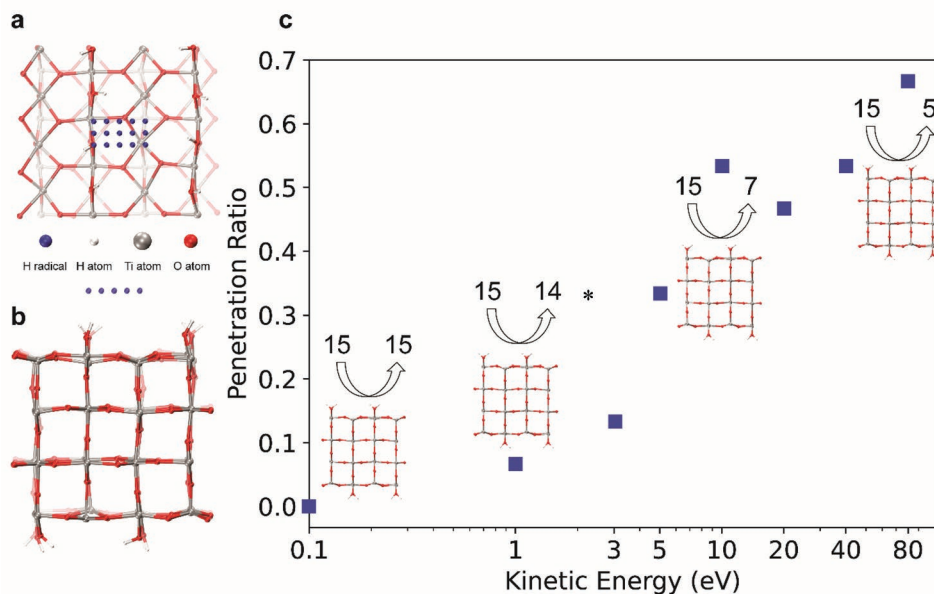


Figure 4. a) Top view of the $\text{TiO}_2(110)$ rutile surface. b) Side view of the employed slab supercell consisting of 4 Ti-O layers representing the $\text{TiO}_2(110)$ surface. c) Penetration ratio of vertically impinging H radicals as a function of initial kinetic energy. White, red, gray, and blue spheres represent H, O, Ti atoms and the initial positions of the H radicals, respectively. * Details see Figure S12, Supporting Information.

Ti^{3+} in the disordered shell which is responsible for the bandgap narrowing (Figure 2h),^[1,6] in agreement with the bandgap value of 2.91 eV from UV-vis spectra (Figure S5, Supporting Information; Table 1), leading to efficient electron-hole pair generation; ii) EELS observes that oxygen vacancies are only formed in the disordered shell (Figure 2e), not only indicating the bulk defect suppression to increase charge transport, but also achieving the largest band bending: photoelectrons from the shell prefer to be transferred into the electrolyte rather than the core when H-TiO₂ nanorods are in contact with the electrolyte because there are no localized states (LS)^[8] formed in the core, resulting in a maximum potential difference, to further promote charge transport and injection. This finding is consistent with a maximum band bending of 1.1 V, which is determined by the highest negative shift in V_{fb} of $-0.30 V_{RHE}$ from M-S plots (Figure 3c; and Figures S7 and S8, Supporting Information). We conclude that the enhanced PEC activity is mainly ascribed to the narrower bandgap, larger band bending, as well as bulk defect suppression.

We experimentally showed that the efficient RRPB enables the synthesis of H-TiO₂ to attain the highest photocurrent density at 5 min, but the mechanism of RRPB remains unclear, which motivates us to study the interaction between kinetic low-energy hydrogen ions and TiO₂ leading to the improved PEC activity.

2.3. DFT Calculations

We employed DFT calculations to evaluate the penetration behavior of kinetic low-energy hydrogen ions into the $\text{TiO}_2(110)$ surface to reveal the mechanisms of RRPB and enhanced PEC performance.

In our previous work,^[6] we have shown that the main bottleneck for a molecular hydrogen treatment from a microscopic

point of view, is the large energy barrier for dissociative H₂ surface adsorption. For atomic hydrogen, the overall reaction barriers for surface adsorption and subsurface diffusion are considerably reduced, resulting in strongly enhanced kinetics of the hydrogen uptake by TiO₂. Still, in the case of rutile TiO₂, our previous DFT results indicate an overall barrier of 0.87 eV for the subsurface diffusion of atomic hydrogen such that thermal activation of this process is required and the hydrogenation speed will in general depend on the substrate temperature.^[6] As demonstrated experimentally in this work, kinetic low-energy hydrogen ions produced by RRPB are highly efficient in penetrating the TiO₂ surface even at room temperature (Table S1, Supporting Information) indicating that thermal activation is not needed.

To investigate the efficiency of H species from RRPB to directly penetrate the $\text{TiO}_2(110)$ surface from a theoretical point of view, we performed ab initio molecular dynamics (AIMD) simulations using DFT. The technical details of the employed DFT approach are given in the Experimental Section. Impinging H radicals with 8 different initial kinetic energies and 15 different initial lateral positions were placed 3 Å above a periodically repeated rutile $\text{TiO}_2(110)$ surface slab that has been equilibrated at a temperature of 500 K in a separate AIMD run prior to the actual impingement simulations. The TiO₂ slabs were generated from a 2×4 surface supercell and comprised 4 Ti-O layers corresponding to a thickness of 1.1 nm, white, red, and gray, blue spheres represent H, O, Ti atoms, and H radical, respectively, see Figure 4a,b. AIMD simulations where the impinging H radical shot through the slab were repeated with slabs consisting of 8 Ti-O layers to investigate the penetration depth as a function of initial kinetic energy (Figure S9, Supporting Information). Within the limits of adiabatic standard DFT calculations, the impinging H radicals will be charge neutral particles in the starting configuration.^[17] But

in a typical hydrogen plasma process, the hydrogen species are composed of energetic H_x^+ ions ($x = 1-3$) and thermal $[H]$ radicals,^[18] for details see the Supporting Information. It is evident that the modeling of plasma hydrogenation is more complex than that of molecular and atomic hydrogenation. However, the modeling of charge neutral H species can be justified by the fact that the energetic H_x^+ ions will decay into energetic charge neutral H radicals upon dissociative recombination close to the surface.^[19] Therefore, the restriction of charge neutrality does not pose a severe limitation.^[19] Experimentally, in our study a self-bias voltage of -250 V was achieved during the RRPB treatment such that the maximum energy of singly charged ions is limited to ≈ 250 eV, although the energy distribution is quite broad.^[20] Among the charged species, H_3^+ ions dominate by far.^[20] Because of the fragmentation of H_3^+ into H radicals close to the surface and taking into account the bonding energy of H_3^+ , we show in the Supporting Information that maximum energies of the relevant H radicals reaching the surface will be around 80.33 eV.^[21] In order to sample the full kinetic energy range in our AIMD simulations, we initialized the velocities of the H radicals along the surface normal to obtain initial kinetic particle energies $E_{kin,0}$ of 0.1, 1, 3, 5, 10, 20, 40, and 80 eV. Additionally, random velocity components perpendicular to the surface normal corresponding to a thermal energy of 500 K were applied for the incoming H radicals. For each of the 8 different kinetic energy values $E_{kin,0}$, a lateral spatial 3×5 grid was used to sample 15 different initial positions of the impinging H radical as shown in Figure 4a,b; and Figure S10 (Supporting Information). For further details concerning the selection of the 15 inequivalent sampling points, see the Supporting Information.

We explored the penetration ratio of the vertically impinging H radicals as a function of $E_{kin,0}$ (Figure 4c; and Figures S11–S18, Supporting Information). For the lowest investigated initial kinetic energy $E_{kin,0} = 0.1$ eV, all 15 H radicals were reflected (Figure S11, Supporting Information) in agreement with our previous study that predicted a minimal energy barrier of 0.87 eV for the subsurface diffusion.^[6] In case of $E_{kin,0} = 1$ eV (Figure S12, Supporting Information), one out of fifteen H radicals could penetrate the TiO_2 surface and finally bonded to one of the three-fold coordinated surface O ions (O_{3c}). Increasing the initial kinetic energy to $E_{kin,0} = 10$ eV (Figure S15, Supporting Information), 7 out of 15 H radicals were reflected and 8 out of 15 H radicals penetrated the TiO_2 surface. It is noted that for low initial kinetic energies of 1, 3, and 5 eV in addition to penetration and reflection also the adsorption of H radicals on the $TiO_2(110)$ surface was observed, for details see Figures S12–S14, Supporting Information. We counted an H radical as penetrating when it either was stopped within the modeled TiO_2 slab or shot through and left the slab on the opposite surface. We note that it does not exclude the scenario where some of the H radicals that penetrated the surface and shot through the slab would have left the surface on the upper side again due to a reversion of the direction of velocity within the TiO_2 system, if thicker slab models had been considered. Therefore, the actual penetration ratios might be somewhat smaller than found in the simulations. At the highest investigated velocity corresponding to $E_{kin,0} = 80$ eV, 10 out of 15 H radicals penetrated the TiO_2 surface corresponding to a penetration ratio of 67% (Figure S18, Supporting Information).

In the other 5 simulations, the impinging H radicals were reflected due to collision with an O or Ti ion of the TiO_2 lattice (Video S1 and Figure S18, Supporting Information). In general, we find that with increasing initial velocity, the ratio of penetrating H radicals tends to increase. Figure 4c shows that H radicals with initial kinetic energies $E_{kin,0} \geq 1$ eV can indeed directly penetrate the TiO_2 surface without thermal activation, and the penetration ratio of H radicals with $E_{kin,0} \geq 10$ eV can reach a value of around 0.5. At this point, it is interesting from a fundamental point of view to contrast the interaction of energetic H particles with TiO_2 surfaces with the thermal H species which dominate atomic and molecular hydrogenation processes.^[4-6] In the case of impinging thermal hydrogen species, a direct hydrogen penetration is not possible. Rather the uptake of hydrogen in the subsurface region requires the two subsequent elementary steps: i) chemisorption and ii) subsurface diffusion. As shown in our previous work,^[6] molecular hydrogen not only has to overcome a considerable energy barrier for dissociative chemisorption but also suitable unoccupied surface sites are required. In principle, free surface sites for the chemisorption of thermal hydrogen only become available when thermally activated and hence sluggish subsurface H diffusion $O_{2c} \rightarrow O_{3c} \rightarrow O_{sub}$ or recombinative dissociation of H_2 molecules occur. The latter process further reduces the hydrogenation efficiency. Atomic hydrogen has more favorable kinetics for the subsurface diffusion $O_{3c} \rightarrow O_{sub}$ compared to molecular hydrogen. Due to the possibility of adsorption at energetically higher lying surface sites, the energy barrier is somewhat lower but still efficient hydrogenation becomes only possible at elevated substrate temperatures.^[6]

In our previous work,^[6] we had shown that the minimal energy barrier for diffusion of a chemisorbed H into the subsurface region is 0.87 eV and proceeds via a path in the vicinity of an O_{3c} surface oxygen ion. For the definition of O_{3c} ions, see Figure S10 (Supporting Information). At the same time the barrier for the chemisorption of an H radical at an O_{3c} surface oxygen ion is small with a value of 0.08 eV.^[6] From this we conclude that the minimal energy path for direct penetration into the subsurface region will also proceed via a path that is closely related to the $O_{3c} \rightarrow O_{sub}$ route. This is also consistent with the only trajectory #8 with $E_{kin,0} = 1$ eV (Figure 5; and Figure S12, Supporting Information) that penetrated the rutile surface, which follows a path in the direct vicinity of an O_{3c} surface ion. With increasing initial kinetic energy also multiple penetration pathways with higher energy barriers around $O_{3c} \rightarrow O_{sub}$ in RRPB become available. This rapidly increases the penetration probability with increasing initial kinetic energy (Figure 5), leading to the highly efficient RRPB. In case of the vertically impinging H radicals shown in Figure 5, the only initial lateral positions where penetration was never observed are those that are directly on top of surface O or Ti ions. Here, direct collisions of the impinging H radical with the surface ions lead to very high energy barriers that even cannot be overcome in the case of the highest investigated initial kinetic energies of 80 eV.

A comparison of the molecular and atomic hydrogenations, along with RRPB from an atomistic point of view is summarized in Table 2, indicating the fast subsurface transport kinetics feature of kinetic low-energy hydrogen ions. Taken together, these results show that the fast subsurface transport

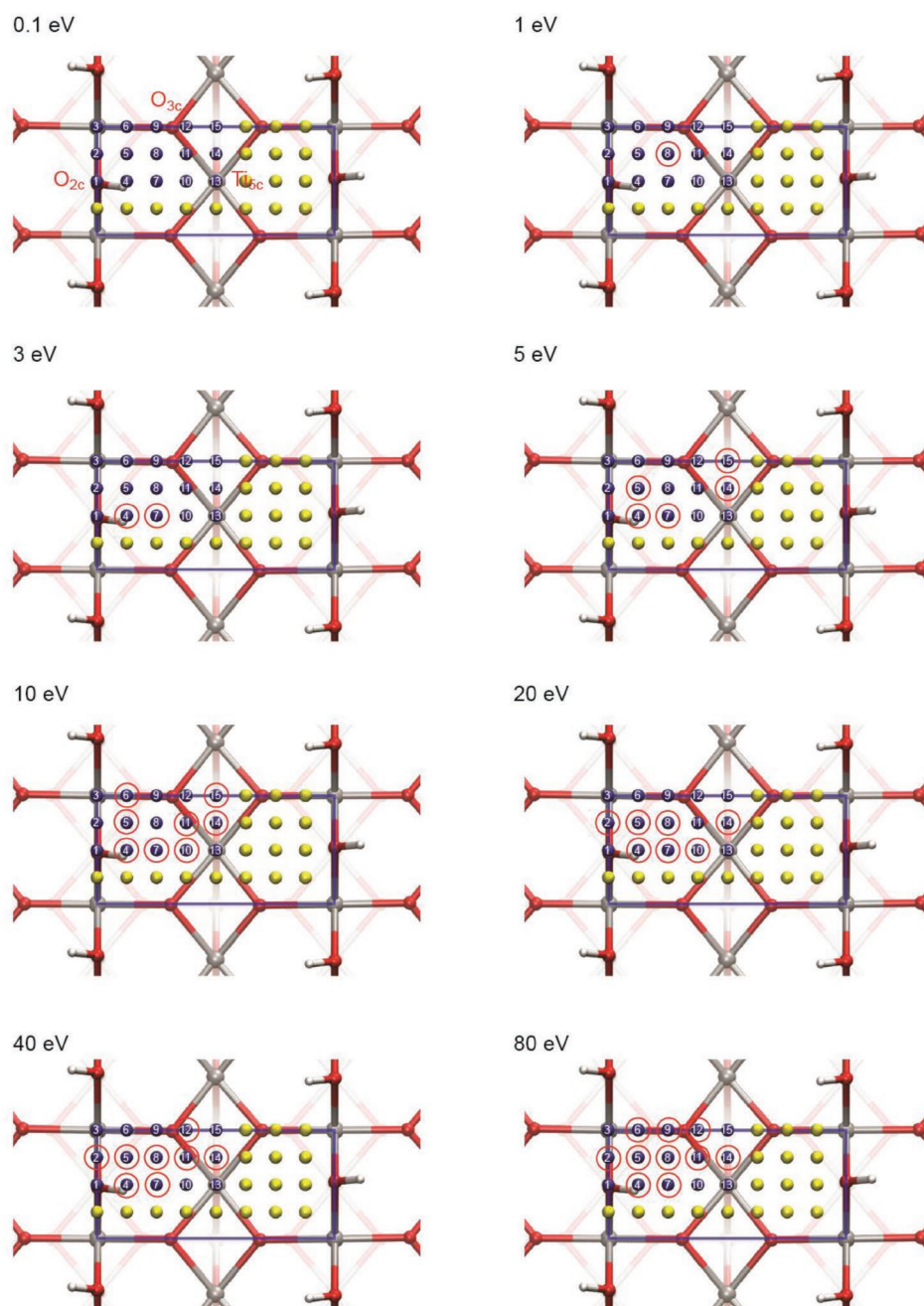


Figure 5. The lateral positions of H radicals with initial kinetic energy of 0.1, 1, 3, 5, 10, 20, 40, and 80 eV that were penetrated the rutile slab. Penetration was never observed for the initial positions of #1, #3, and #13 that are directly on top of surface O or Ti ions.

Table 2. Factors influence the efficiency and kinetics of the different hydrogenation methods based on thermal molecular hydrogen H_2 , thermal atomic hydrogen [H], and energetic hydrogen ions H^+ from RRP.

Hydrogenation species	H_2	[H]	H^+
Surface adsorption kinetics (Energy barrier [eV])	Slow (1.86)	Fast (0.08)	Not relevant
Surface adsorption sites	O_{2c}	O_{3c}	Not relevant
Subsurface transport pathway	$O_{2c} \rightarrow O_{3c} \rightarrow O_{sub}$	$O_{3c} \rightarrow O_{sub}$	Multiple penetration pathways
Subsurface transport kinetics (Energy barrier [eV])	Slow (1.66)	Intermediate (0.87)	Fast No thermal activation needed for subsurface diffusion

enables kinetic low-energy hydrogen ions to directly penetrate into TiO₂ subsurface via multiple penetration pathways without the need of thermal activation, leading to efficient RRPB.

Moreover, we analyzed the penetration depth of those H radicals that were not reflected or adsorbed, as a function of $E_{\text{kin},0}$. Typical trajectories from AIMD simulations of H radicals impinging with energies 0.1, 1, 10, 20, 40, and 80 eV are presented in **Figure 6a–f**; and Videos S2–S7, Supporting Information. The penetration depth was determined as the distance from the TiO₂ surface after the H radical came to a halt. An impinging H radical was considered as being trapped when its kinetic energy reached values constantly below 0.5 eV (see the Experimental Section). The structure of the TiO₂ surface slab containing 8 Ti–O layers is shown in **Figure 6g**. All simulations where the impinging H radicals shot through the slab with 8 Ti–O layers, i.e., where the H radical was not stopped within the slab model, are indicated by open circles and arrows at the bottom of the plot. Simulation results where the impinging H radicals were reflected and adsorbed are shown in **Figures S11–S18**, Supporting Information. Due to the sampling of different initial lateral positions, more than one data point is usually shown for each kinetic energy value, details see **Figures S11–S18**, Supporting Information. The penetration depths as a function of $E_{\text{kin},0}$ of the various simulations are shown in **Figure 6g**. Up to initial kinetic energies of 10 eV, the maximally obtained penetration depths did not exceed 1.0 nm corresponding to the fourth Ti–O layer from the surface as shown in **Figure 6a–c**. At these lower kinetic energies, indeed most of the H radicals penetrating the surface were stopped at the first or second Ti–O layer by bonding to an O ion. As the example simulation shown in **Figure 6d** demonstrates, at $E_{\text{kin},0} = 20$ eV generally larger penetration depths were observed compared to the simulations with lower initial kinetic energies and both stopping of the H radicals within the TiO₂ slabs, and through-shot events were detected (**Figure 6g**). At high initial kinetic energies of 40 and 80 eV, for example trajectories see **Figure 6e,f**, all H radicals which were not reflected shot through the TiO₂ slab even if the thicker slab with 8 Ti–O layers and a dimension of 2.3 nm in the direction along the surface normal was used in the AIMD simulations. It is concluded that when the kinetic energy of H radical is lower than 10 eV, the penetration depths are less than 1 nm; when the kinetic energy is increased to 20 eV, the penetration depths increase to 1–2 nm, some are larger than 2.3 nm; when the kinetic energy further increases to 40 or 80 eV, all penetration depths are larger than 2.3 nm. Our experimental results and our previous ab initio study^[6] clearly demonstrate that the surface hydrogenation induces disorder in the rutile phase such that the straight channel structures in which the highly energetic hydrogen species can travel with low energy losses will disappear during the hydrogenation process. This means that also vertically impinging hydrogen radicals with higher kinetic energies of up to 80 eV which penetrate the TiO₂ surface will be quickly stopped or reflected upon collision with Ti and O ions of the TiO₂ disordered structure. Moreover, we expect that H radicals impinging with an angle of incidence significantly different from 0° will be more prone to strong ion-ion collisions and hence will have a much weaker tendency to channel even in the fully crystalline rutile lattice. Therefore, we assume that

the penetration depth of hydrogen radicals larger than 2.3 nm with higher kinetic energies > 20 eV is severely overestimated in our DFT calculations.

In order to investigate whether penetration of the rutile TiO₂ surface requires vertically impinging H species at angle of incidence of 0° or is also feasible at angles deviating from 0°, additional DFT MD simulations with angle of incidence of 5°, 15°, 30°, 45°, 60°, and 75° were performed (**Figures S19–S25**, Supporting Information) for H radicals with $E_{\text{kin},0} = 10$ eV. It is shown that penetration can be even observed at an angle of incidence of 60° (**Figures S19 and S24**, Supporting Information), demonstrating that a vertical impingement is not a precondition to have an efficient uptake of kinetic H radicals.

To explore the subsurface transport of H radicals finally resulting in the formation of OH bonds, the kinetic energy along the trajectories of the impinging H radicals was analyzed (**Figures S26 and S27**, Supporting Information). It is shown that the trajectories of the impinging H radicals before trapping are in general characterized by frequent collisions with the Ti and O ions of the rutile lattice in the subsurface region leading to rapid dissipation of the kinetic energy and finally to the formation of OH bonds which contribute to the formation of a controllable disordered shell. In total we find that impinging H radicals with sufficient initial kinetic energy $E_{\text{kin},0} \geq 1$ eV have a high probability of directly penetrating the TiO₂ rutile surface and that the kinetic energy is efficiently dissipated within the subsurface region. This can explain the efficient hydrogenation of our RRPB close to the surface.

The shallow penetration depth feature of low-energy hydrogen ions revealed by our DFT is confirmed by a reported work where Ohashi et al. used low-energy hydrogen ions of 500 eV to treat the TiO₂(110) surface and found that the H depth profile showed a shallow peak at about 1 nm penetration depth.^[22] It indicates that low-energy hydrogen ions of up to 80.33 eV generated in our RRPB process likewise lead to shallow penetration depth, a feature that allows them to controllably interact with TiO₂ to attain the controllable disordered shell and bulk defect suppression, ultimately contributing to the enhanced PEC performance, in agreement with the hydrogenation-property experiments.

2.4. Efficient RRPB versus State-of-the-Art Hydrogenations

The RRPB shows the following unique features:

i. Efficient hydrogenation via fast subsurface transport kinetics

Chen et al. fabricated H-TiO₂ nanoparticle in 20 bar of H₂ at 200 °C for 5 days,^[4] and Wang et al. synthesized the H-TiO₂ nanorods in 1 bar of H₂ at 400 °C for 1 h,^[5] but high temperature and prolonged treatment time are needed for the molecular hydrogenation. Alternatively, Xu et al. used Pd to dissociate molecular hydrogen into atomic hydrogen to prepare H-TiO₂ at 250 °C for 10 min, but noble metal particles and high temperature are required for the atomic hydrogenation.^[9] The inefficient molecular and atomic hydrogenations are due to their intrinsic reaction mechanism with TiO₂: thermal activation via high temperature is required to overcome the energy barriers of

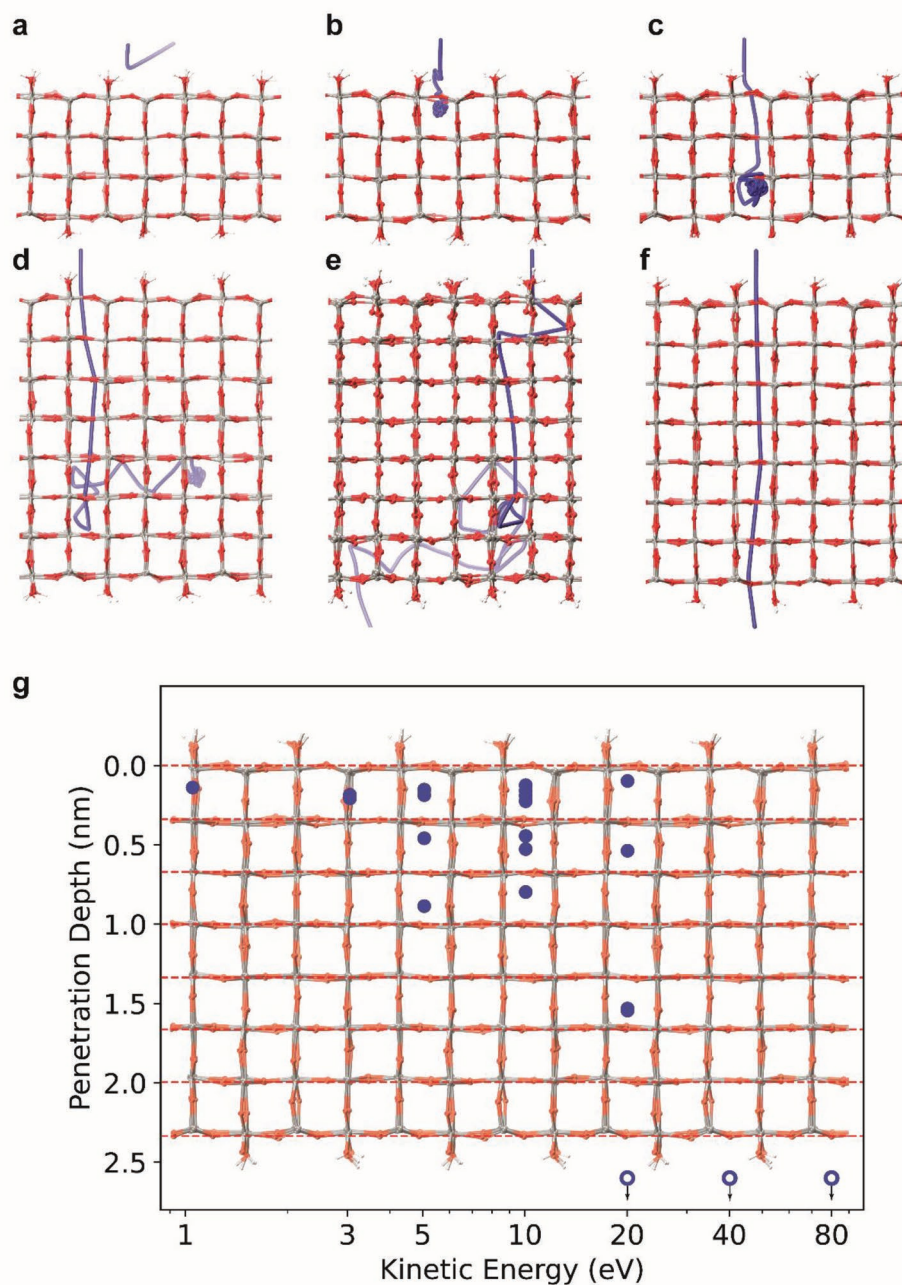


Figure 6. a–f) Typical trajectory of an H radical impinging the TiO₂ surface with a kinetic energy of 0.1, 1, 10, 20, 40, and 80 eV, respectively. g) Penetration depth of vertically impinging H radicals as a function of initial kinetic energy.

chemisorption and subsurface diffusion to penetrate the TiO₂ surface. Simultaneously, Wang et al. reported for the first time the application of hydrogen plasma at a RF power of 200 W to treat TiO₂ nanoparticles at 500 °C for 4 h,^[12] and Lepcha et al. prepared H-TiO₂ nanofibers by applying a high temperature of 500 °C and RF power of 15 W,^[13] which shows that conventional plasma hydrogenations operate at high power or high temperature set by the plasma equipment to provide high-energy hydrogen ions to deeply penetrate the TiO₂, causing uncontrollable plasma hydrogenation. In our work, the RRP strategy achieves kinetic low-energy hydrogen ions, which can directly penetrate into the TiO₂

subsurface to efficiently prepare H-TiO₂ at room temperature due to the fast subsurface transport kinetics.

ii. Controllable hydrogenation via shallow penetration depth

The feature of shallow penetration depth is difficult to be realized by conventional plasma hydrogenations, to the best of our knowledge, it is reported for the first time in this work. Liang et al. fabricated H-TiO₂ films by high power of 380 W to gain low photocurrent density of 0.67 mA cm⁻² at 1.23 V_{RHE},^[15] and Tian et al. applied RF power of 200 W and high temperature of 425 °C to hydrogenate TiO₂ nanorods obtaining the

photocurrent density of 0.9 mA cm⁻² at 1.23 V_{RHE},^[14] however, due to the deep penetration depth, high-energy hydrogen ions provided by conventional plasma hydrogenations result in the formation of recombinative bulk defects and hence in poor PEC activity. Due to the shallow penetration depth of low-energy hydrogen ions, our RRP strategy can not only synthesize H-TiO₂ with a controllable disordered shell but also suppresses bulk defects to trigger enhanced PEC activity, exhibiting the highest photocurrent density of 2.55 mA cm⁻² at 1.23 V_{RHE}, which demonstrates the advance of the RRP over state-of-the-art hydrogenations (Figure S28, Supporting Information).

iii. Stable and upscalable hydrogenation without FTO degradation

The photocurrent density at 1.23 V_{RHE} of H-TiO₂ at 5 min measured at different times (Figure S29, Supporting Information) shows that over 95% of the initial photocurrent density are retained following 1 year of ambient air storage, indicating the robust and excellent stability of H-TiO₂ at 5 min. In our RRP, the substrate electrode with diameter of 100 mm shows the potential for large-scale hydrogenation (Figure S1, Supporting Information). Table S4 (Supporting Information) shows no degradation issue of FTO after the RRP process. All features indicate that the RRP approach is suitable for device applications.

iv. Broad scope of applications

The interaction of hydrogen with the TiO₂ surface, especially the penetration of hydrogen into the TiO₂ subsurface is an important topic for different catalytic processes like water splitting and hydrogen storage.^[1-4,6,9-11] Our detailed study of low-energy hydrogen ions penetrating into TiO₂ subsurface can help to understand the origins of these phenomena. Due to the mild hydrogenation conditions without high temperature, high power and noble metal catalysts, our RRP can not only fabricate H-TiO₂ to achieve enhanced PEC performance, but also hydrogenate other oxides to tune material properties, such as Mott transition, phase modulation, and magnetic anisotropy for various practical applications.^[23-25]

3. Conclusions

We developed an efficient RRP strategy by integrating a circular electromagnetic coil, which yields low-energy hydrogen ions to prepare H-TiO₂ nanorods with controllable disordered shell due to efficient H doping of TiO₂ through the following steps: fast subsurface transport of H radicals is promoted via unique multiple penetration pathways around the O_{3c} → O_{sub} route, resulting in frequent collisions of H radicals with Ti and O ions in the TiO₂ lattice. This leads to rapid dissipation of the kinetic energy and fast oscillations of H radicals to form more OH bonds. We demonstrated that the resulting H-TiO₂ exhibits a high photocurrent density of 2.55 mA cm⁻² at 1.23 V_{RHE} and retains excellent stability over 95% of initial photocurrent density following 1 year of ambient air storage, superior to that of prior reported H-TiO₂. By uniting hydrogenation-property experiments with DFT calculations, we found that the efficient RRP and improved PEC activity originate from kinetic low-energy hydrogen ions featuring fast subsurface transport kinetics and shallow penetration depth. These hydrogenation

characteristics contribute to narrower bandgap and larger band bending, along with a beneficial suppression of bulk defects. Overall, this work showcases a promising strategy to hydrogenate TiO₂ and other oxides for a wide variety of applications and provides valuable insight into understanding the underlying hydrogenation mechanisms and improved properties.

4. Experimental Section

Growth of TiO₂ Nanorod Arrays on FTO (F:SnO₂) Substrate: TiO₂ nanorods were grown on a FTO substrate by hydrothermal method.^[26] Typically, 0.35 mL of tetra-tert-butoxy titanate (Ti(O^tBu)₄) was dissolved in 30 mL of 6 M HCl, and the solution was transferred into a steel-lined Teflon autoclave, where a cleaned FTO substrate was placed. The autoclave was maintained at 160 °C for 18 h, then the coated FTO substrate was washed several times with deionized water and ethanol, and dried in air. To remove the chemical residues and improve the crystallinity of TiO₂ nanorods and their electric contacts with FTO glass, the samples were annealed at 550 °C for 3 h in air.

Hydrogenation of TiO₂ Nanorods by RRP: Figure 1a and Figure S1 (Supporting Information) show the RRP set-up including an integrated circular electromagnetic coil. The RRP processing parameters such as RF power, pressure, treatment time, and hydrogen gas flow were controlled precisely by a programmable recipe. Therefore, reproducible hydrogenation of TiO₂ nanorods at different treatment times can be achieved (Table S1, Supporting Information).

Characterizations of the Samples: The H-TiO₂ nanorods were investigated by using SEM Zeiss Supra 35, Empyrean XRD (Cu K_α), CARY-500 UV-VIS spectrometer, and HR-TEM Jeol J2010F FEG operating at 200 kV and coupled to a Gatan imaging filter (GIF) spectrometer, and Thermo Scientific K-Alpha XPS system (Al K_α).

PEC Studies: A Newport solar simulator 150 W Xe lamp with AM 1.5 G filter acted as a light source for the PEC investigation. All photocurrent density versus potential (*J*-*V*) curves were recorded with a Princeton Applied Research 2273 potentiostat using 1 M KOH as electrolyte in a three-electrode configuration, in which Ag/AgCl in 3 M KCl was the reference electrode, and platinum wire was the counter electrode. The IPCE was performed based on Newport Oriol QE-PV-SI and CHI660E electrochemical workstations. The M-S measurements were performed on the Gamry electrochemical workstation.

The conversion from Ag/AgCl to RHE potential is given as follows:

$$E(\text{RHE}) = E(\text{Ag/AgCl}) + 0.059\text{pH} + E_0(\text{Ag/AgCl}) \quad (4)$$

where $E_0(\text{Ag/AgCl}) = 0.1976$ V versus normal hydrogen electrode (NHE) at 25 °C and $E(\text{Ag/AgCl})$ is our used working potential.

DFT Calculations: We used the Vienna ab initio simulations package (VASP).^[27] VASP uses a plane wave basis set in order to describe the valence electrons. The Kohn-Sham wavefunctions of the valence electrons were expanded in a plane wave basis set using a cut-off energy of 400 eV for the ab initio molecular dynamics (AIMD) simulations and of 550 eV for structural relaxations. The projector-augmented wave method (PAW) was employed to take into account the effect of core electrons.^[28,29] Standard semilocal DFT functionals tend to underestimate correlation effects due to the localized Ti 3d electrons. To partially correct these deficiencies, a Hubbard term was applied according to the DFT + U scheme of Dudarev et al.^[30] Here, we combined the Hubbard correction with the semilocal PBE functional.^[31] As Hubbard U parameter we used 4.0 eV following previous studies of defective rutile TiO₂ surfaces.^[32,33] In all simulations spin polarized DFT calculations were performed except for the AIMD simulations of the 8 Ti-O layer thick slabs where spin-paired calculations had to be made for convergence reasons.

Ab initio molecular dynamics simulations were performed by combining the VASP calculations of the atomic forces with the integration of Newton's equation of motion using the velocity Verlet

algorithm as implemented in the Atomic Simulation Environment.^[34] Due to the small-time scales of the AIMD simulations, no thermostat was employed, i.e., the NVE ensemble was used. Prior to the simulation of the impingement of H radicals on the rutile surface, the slab systems were equilibrated at a temperature of 500 K. For this purpose, the atom velocities in the fully relaxed slabs were initialized according to the Maxwell–Boltzmann distribution with a temperature of 1000 K. In accordance with the equipartition theorem this resulted after a short AIMD run of 1 ps in an equilibrium temperature of 500 K.

Due to the high speed of the impinging energetic H radicals, small time steps dt had to be used in the initial phase of the AIMD simulations, whereas longer time steps could be used once the H radical had been slowed down within the rutile structure. In detail, the initial time step dt was chosen such that the maximum displacement of the impinging H radicals was equal to $d x_{\max} = 0.02\text{\AA}$. Hence $dt = dx_{\max}/v_0$, where v_0 is the initial velocity of the impinging H radical. The time step in the AIMD simulations was then adapted after every 1000 simulation steps according to $dt = dx_{\max}/v_{\max3}$, where $v_{\max3}$ is the maximum atomic velocity encountered in the last third of the previous simulation period. The simulations were continued until either i) $v_{\max3}$ was below 9780 m s^{-1} corresponding to a kinetic energy of the impinging H radical of less than 0.5 eV or ii) the impinging H radical shot through the rutile slab, i.e., left the slab at the bottom surface. We note that $v_{\max3} < 9780\text{ m s}^{-1}$ means that in the AIMD simulations the kinetic energy of the impinging H radical is less than 0.5 eV for at least 68 fs. For comparison, OH stretching modes in TiO_2 typically have a frequency of 3300 cm^{-1} , corresponding to a period of 10 fs.^[35]

Supporting Information

Supporting Information is available from the Wiley Online Library or from the author.

Acknowledgements

The authors thank Dr. H. Zhou from TU Braunschweig for XRD measurement, Dr. Y. Lin from Hong Kong University of Science and Technology for IPCE measurement, Dr. C. Fabrega from University of Barcelona, Dr. S. Murcia and Dr. T. Andreu from IREC Catalonia Institute for Energy Research for M–S measurement, and Prof. F. Peiró from University of Barcelona for discussions on the TEM/EELS results. The authors gratefully acknowledge the Gauss Centre for Supercomputing e.V. (www.gauss-centre.eu) for funding this project by providing computing time through the John von Neumann Institute for Computing (NIC) on the GCS Supercomputer JUWELS at Jülich Supercomputing Centre (JSC).

Conflict of Interest

The authors declare no conflict of interest.

Data Availability Statement

The data that support the findings of this study are available from the corresponding author upon reasonable request.

Keywords

black titania, low-energy hydrogen ions, multiple penetration pathways, rapid plasma hydrogenation, room-temperature hydrogenation, solar water splitting

Received: July 6, 2022
Revised: September 1, 2022
Published online:

- [1] X. Liu, G. Zhu, X. Wang, X. Yuan, T. Lin, F. Huang, *Adv. Energy Mater.* **2016**, *6*, 1600452.
- [2] W. Zhang, H. He, H. Li, L. Duan, L. Zu, Y. Zhai, W. Li, L. Wang, H. Fu, D. Zhao, *Adv. Energy Mater.* **2021**, *11*, 2003303.
- [3] J. Kang, Y. Zhang, Z. Chai, X. Qiu, X. Cao, P. Zhang, G. Teobaldi, L.-M. Liu, L. Guo, *Adv. Mater.* **2021**, *33*, 2100407.
- [4] X. Chen, L. Liu, P. Y. Yu, S. S. Mao, *Science* **2011**, *331*, 746.
- [5] G. Wang, H. Wang, Y. Ling, Y. Tang, X. Yang, R. C. Fitzmorris, C. Wang, J. Z. Zhang, Y. Li, *Nano Lett.* **2011**, *11*, 3026.
- [6] X. Wang, L. Mayrhofer, M. Hofer, S. Estrade, L. Lopez-Conesa, H. Zhou, Y. Lin, F. Peiró, Z. Fan, H. Shen, L. Schaefer, M. Moseler, G. Braeuer, A. Waag, *Adv. Energy Mater.* **2019**, *9*, 1900725.
- [7] a) Z. Tian, P. Zhang, P. Qin, D. Sun, S. Zhang, X. Guo, W. Zhao, D. Zhao, F. Huang, *Adv. Energy Mater.* **2019**, *9*, 1901287. b) Z. Ma, K. Song, T. Zhang, B. Tang, G. Shao, H. Hou, W. Yang, *Chem. Eng. J.* **2022**, *430*, 132936. c) K. Song, F. He, E. Zhou, L. Wang, H. Hou, W. Yang, *J. Energy Chem.* **2022**, *68*, 49. d) Z. Liang, D. Chen, S. Xu, Z. Fang, L. Wang, W. Yang, H. Hou, *J. Mater. Chem. C* **2021**, *9*, 12263. e) Z. Ma, H. Hou, K. Song, Z. Fang, L. Wang, F. Gao, W. Yang, B. Tang, Y. Kuang, *Chem. Eng. J.* **2020**, *379*, 122266. f) Z. Ma, K. Song, L. Wang, F. Gao, B. Tang, H. Hou, W. Yang, *ACS Appl. Mater. Interfaces* **2019**, *11*, 889.
- [8] Y. Yang, G. Liu, J. T. S. Irvine, H.-M. Cheng, *Adv. Mater.* **2016**, *28*, 5850.
- [9] Y. Xu, C. Zhang, L. Zhang, X. Zhang, H. Yao, J. Shi, *Energy Environ. Sci.* **2016**, *9*, 2410.
- [10] L. Xie, Q. Zhu, G. Zhang, K. Ye, C. Zou, O. V. Prezhdo, Z. Wang, Y. Luo, J. Jiang, *J. Am. Chem. Soc.* **2020**, *142*, 4136.
- [11] G. Jia, Y. Wang, X. Cui, H. Zhang, J. Zhao, L. H. Li, L. Gu, Q. Zhang, L. Zheng, J. Wu, Q. Wu, D. J. Singh, W. Li, L. Zhang, W. Zheng, *Matter* **2022**, *5*, 206.
- [12] Z. Wang, C. Yang, T. Lin, H. Yin, P. Chen, D. Wan, F. Xu, F. Huang, J. Lin, X. Xie, M. Jiang, *Adv. Funct. Mater.* **2013**, *23*, 5444.
- [13] A. Lepcha, C. Maccato, A. Mettenböcker, T. Andreu, L. Mayrhofer, M. Walter, S. Olthof, T.-P. Ruoko, A. Klein, M. Moseler, K. Meerholz, J. R. Morante, D. Barreca, S. Mathur, *J. Phys. Chem. C* **2015**, *119*, 18835.
- [14] Z. Tian, H. Cui, G. Zhu, W. Zhao, J. Xu, F. Shao, J. He, F. Huang, *J. Power Sources* **2016**, *325*, 697.
- [15] J. Liang, N. Wang, Q. Zhang, B. Liu, X. Kong, C. Wei, D. Zhang, B. Yan, Y. Zhao, X. Zhang, *Nano Energy* **2017**, *42*, 151.
- [16] Y. Madhavi, P. Kondaiah, M. Ghosh, G. M. Rao, *Ceram. Int.* **2020**, *46*, 17791.
- [17] B. Kaduk, T. Kowalczyk, T. van Voorhis, *Chem. Rev.* **2012**, *112*, 321.
- [18] E. Despiou-Pujo, A. Davydova, G. Cunge, D. B. Graves, *Plasma Chem. Plasma Process.* **2016**, *36*, 213.
- [19] E. Despiou-Pujo, A. Davydova, G. Cunge, L. Delfour, L. Magaud, D. B. Graves, *J. Appl. Phys.* **2013**, *113*, 114302.
- [20] A. Felten, D. McManus, C. Rice, L. Nittler, J.-J. Pireaux, C. Casiraghi, *Appl. Phys. Lett.* **2014**, *105*, 183104.
- [21] B. J. McCall, A. J. Huneycutt, R. J. Saykally, N. Djuric, G. H. Dunn, J. Semaniak, O. Novotny, A. Al-Khalili, A. Ehlerding, F. Hellberg, S. Kalhori, A. Neau, R. D. Thomas, A. Paal, F. Österdahl, M. Larsson, *Phys. Rev. A* **2004**, *70*, 052716.
- [22] Y. Ohashi, N. Nagatsuka, S. Ogura, K. Fukutani, *J. Phys. Chem. C* **2019**, *123*, 10319.
- [23] Y. Zhou, X. Guan, H. Zhou, K. Ramadoss, S. Adam, H. Liu, S. Lee, J. Shi, M. Tsuchiya, D. D. Fong, S. Ramanathan, *Nature* **2016**, *534*, 231.
- [24] H. Yoon, M. Choi, T.-W. Lim, H. Kwon, K. Ihm, J. K. Kim, S.-Y. Choi, J. Son, *Nat. Mater.* **2016**, *15*, 1113.
- [25] H. Jani, J. Linghu, S. Hooda, R. V. Chopdekar, C. Li, G. J. Omar, S. Prakash, Y. Du, P. Yang, A. Banas, K. Banas, S. Ghosh, S. Ojha, G. R. Umapathy, D. Kanjilal, A. Ariando, S. J. Pennycook, E. Arenholz, P. G. Radaelli, J. M. D. Coey, Y. P. Feng, T. Venkatesan, *Nat. Commun.* **2021**, *12*, 1668.

- [26] X. Feng, K. Shankar, O. K. Varghese, M. Paulose, T. J. Latempa, C. A. Grimes, *Nano Lett.* **2008**, *8*, 3781.
- [27] G. Kresse, J. Furthmüller, *Phys. Rev. B* **1996**, *54*, 11169.
- [28] G. Kresse, D. Joubert, *Phys. Rev. B* **1999**, *59*, 1758.
- [29] P. E. Blöchl, *Phys. Rev. B* **1994**, *50*, 17953.
- [30] S. L. Dudarev, G. A. Botton, S. Y. Savrasov, C. J. Humphreys, A. P. Sutton, *Phys. Rev. B* **1998**, *57*, 1505.
- [31] J. P. Perdew, K. Burke, M. Ernzerhof, *Phys. Rev. Lett.* **1996**, *77*, 3865.
- [32] B. J. Morgan, G. W. Watson, *Surf. Sci.* **2007**, *601*, 5034.
- [33] H. P. Pinto, G. H. Enevoldsen, F. Besenbacher, J. V. Lauritsen, A. S. Foster, *Nanotechnology* **2009**, *20*, 264020.
- [34] A. Hjorth Larsen, J. Jørgen Mortensen, J. Blomqvist, I. E. Castelli, R. Christensen, M. Duřak, J. Friis, M. N. Groves, B. Hammer, C. Hargus, E. D. Hermes, P. C. Jennings, P. Bjerre Jensen, J. Kermode, J. R. Kitchin, E. Leonhard Kolsbjerg, J. Kubal, K. Kaasbjerg, S. Lysgaard, J. Bergmann Maronsson, T. Maxson, T. Olsen, L. Pastewka, A. Peterson, C. Rostgaard, J. Schiøtz, O. Schütt, M. Strange, K. S. Thygesen, T. Vegge, et al., *J. Phys.: Condens. Matter* **2017**, *29*, 273002.
- [35] W. R. Palfey, G. R. Rossman, W. A. Goddard, *J. Phys. Chem. Lett.* **2021**, *12*, 10175.